crystals

MDPI

Article

Simulation of High Breakdown Voltage, Improved Current Collapse Suppression, and Enhanced Frequency Response AlGaN/GaN HEMT Using A Double Floating Field Plate

Peiran Wang [1], Chenkai Deng [1], Hongyu Cheng [1], Weichih Cheng [1], Fangzhou Du [1], Chuying Tang [1], Chunqi Geng [2], Nick Tao [2], Qing Wang [1,3,4,*] and Hongyu Yu [1,3,4,*]

[1] School of Microelectronics, Southern University of Science and Technology, Shenzhen 518055, China
[2] Maxscend Microelectronics Company Limited, Wuxi 214072, China
[3] Engineering Research Center of Integrated Circuits for Next-Generation Communications, Ministry of Education, Southern University of Science and Technology, Shenzhen 518055, China
[4] GaN Device Engineering Technology Research Center of Guangdong, Southern University of Science and Technology, Shenzhen 518055, China
* Correspondence: wangq7@sustech.edu.cn (Q.W.); yuhy@sustech.edu.cn (H.Y.)

Abstract: In this paper, DC, transient, and RF performances among AlGaN/GaN HEMTs with a no field plate structure (basic), a conventional gate field plate structure (GFP), and a double floating field plate structure (2FFP) were studied by utilizing SILVACO ATLAS 2D device technology computer-aided design (TCAD). The peak electric fields under the gate in drain-side can be alleviated effectively in 2FFP devices, compared with basic and GFP devices, which promotes the breakdown voltage (BV) and suppresses the current collapse phenomenon. As a result, the ON-resistance increase caused by the current collapse phenomena is dramatically suppressed in 2FFP ~19.9% compared with GFP ~49.8% when a 1 ms duration pre-stress was applied with V_{ds} = 300 V in the OFF-state. Because of the discontinuous FP structure, more electric field peaks appear at the edge of the FFP stacks, which leads to a higher BV of ~454.4 V compared to the GFP ~394.3 V and the basic devices ~57.6 V. Moreover, the 2FFP structure performs lower a parasitic capacitance of C_{gs} = 1.03 pF and C_{gd} = 0.13 pF than those of the GFP structure (i.e., C_{gs} = 1.89 pF and C_{gd} = 0.18 pF). Lower parasitic capacitances lead to a much higher cut-off frequency (f_t) of 46 GHz and a maximum oscillation frequency (f_{max}) of 130 GHz than those of the GFP structure (i.e., f_t = 27 GHz and f_{max} = 93 GHz). These results illustrate the superiority of the 2FFP structure for RF GaN HEMT and open up enormous opportunities for integrated RF GaN devices.

Keywords: AlGaN/GaN high-electron mobility transistors (HEMTs); floating field plate (FFP); breakdown voltage; current collapse; frequency response; TCAD

Citation: Wang, P.; Deng, C.; Cheng, H.; Cheng, W.; Du, F.; Tang, C.; Geng, C.; Tao, N.; Wang, Q.; Yu, H. Simulation of High Breakdown Voltage, Improved Current Collapse Suppression, and Enhanced Frequency Response AlGaN/GaN HEMT Using A Double Floating Field Plate. *Crystals* **2023**, *13*, 110. https://doi.org/10.3390/cryst13010110

Academic Editor: Ray-Hua Horng

Received: 19 December 2022
Revised: 26 December 2022
Accepted: 4 January 2023
Published: 7 January 2023

1. Introduction

AlGaN/GaN-based high-electron mobility transistors (HEMTs) are highly promising for high frequency and high voltage applications relying on a high electron saturation velocity, high critical electric field (3.3 MV/cm), and high electron mobility as well as a high channel carrier density induced by the piezoelectric and spontaneous polarization effects [1–4]. However, major obstacles for radio frequency GaN HEMT are the limited breakdown voltage, increased parasitic capacitance, and the severe current collapse phenomenon due to the shortening of channel length with the device size scaling down [5–8]. Breakdown voltage enhanced by applying a conventional gate field plate structure is restricted and the f_t and f_{max} degradation will also appear on account of extra parasitic capacitances C_{gs} and C_{gd} induced by the extended metal material of continuous FP. The breakdown voltage improvement of radio frequency size GaN HEMTs with reduced current collapse phenomenon and maintained RF characteristics are pressing and significant.

Recently, researchers have improved the device's breakdown and current collapse suppression characteristics by a series of methods. The high electric breakdown enables high-voltage operation and improves the efficiency. To enhance the device's performance, increasing the breakdown voltage is necessary, and many forms of technology have been reported and developed to achieve this goal. The BV of GaN HEMT is improved by incorporation of conventional GFP [9], a source field plate (SFP) [10], a drain field plate (DFP) [11], multiple grating field plates [12], a buried p-type layer [13], acceptor doping in the buffer layer [14], a back barrier structure [15,16], a quantum well plate (QWP) structure [17], a local charge compensation trench (LCCT) [18], and a recessed floating field plate (RFFP) structure [19]. Thereafter, enormous amounts of literature have been published on FP-based AlGaN/GaN HEMTs in which the features of FP architectures including reliability, design optimization, and the BV increased mechanism have been investigated [20–22]. FP-alleviated current collapse phenomena and mechanisms are reported as well [23–27]. For RF devices, parasitic capacitances are increased by FP structures inevitably which will directly degrade the RF characteristics of devices such as f_t and f_{max}. The FFP structure is based on the grating gate FP structure without biasing applied on each FFP stack. However, a systematic study of the effects of FFP on its breakdown, current collapse phenomena, and frequency response characteristics are lacking.

In this work, we systematically investigate the breakdown, current collapse and RF characteristics of the basic, GFP, and 2FFP structure AlGaN/GaN HEMTs by utilizing TCAD SILVACO ATLAS simulation tools [28] after geometry parameters optimization including the thickness of gate, the effective length of FP, and the quantity of FFP stacks of HEMTs. Subsequently, we demonstrate a radio frequency size 2FFP structure HEMT with excellent breakdown performance, current collapse suppression, and RF characteristics. The devices present a high BV of 454.4 V, an excellent current collapse suppression effect, the parasitic capacitances C_{gs} ~1.03 pF and C_{gd} ~0.13 pF, along with a high f_t and f_{max} of 46 GHz and 130 GHz, respectively. Moreover, the GFP structure HEMTs on the condition that the BV performance is optimized the best are also studied for making comparisons with the 2FFP structure. Compared with the JFOM of the GFP device, which is 10.65 THz·V, the proposed 2FFP device performs almost two times better in terms of the JFOM (i.e., JFOM of 2FFP = 20.90 THz·V). Besides much higher BV, 2FFP devices have a more outstanding current collapse suppression ability and capability of resistance to RF characteristics' degradation, which reveals the extraordinary potential of the 2FFP structure compared to the GFP structure as an efficient comprehensive performance improvement scheme applied in RF GaN HEMT devices.

2. Device Structure Design and Simulation Setup

The basic, GFP, and 2FFP structures implemented for TCAD simulations are shown in Figure 1a–c. The AlGaN/GaN HEMT consists of a 15 nm i-$Al_{0.23}Ga_{0.77}N$ barrier layer with a 35 nm i-GaN channel layer, a 1 μm $Al_{0.05}Ga_{0.95}N$ buffer layer, a 0.3 μm Si_3N_4 passivation layer, and a sapphire substrate. The device under simulating features a gate length (L_G) of 0.1 μm, a gate–source distance (L_{GS}) of 0.5 μm, and a gate–drain distance (L_{GD}) of 2.5 μm.

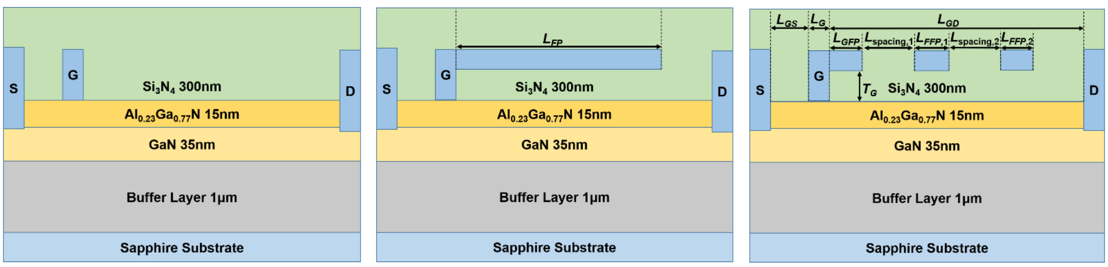

(**a**) (**b**) (**c**)

Figure 1. Cross-section of (**a**) the basic structure, (**b**) the GFP structure, and (**c**) the 2FFP structure AlGaN/GaN HEMTs.

Calibration is a necessary process for III–V compound simulation processes. In this simulation work, the semiconductor parameters of the GaN and AlGaN material are setup as shown in Table 1 according to the calibration results from the works of Karmalkar et al. [9]. In addition, the important models such as the IMPACT SELB model and POLARIZATION models are calibrated as well to make sure the breakdown characteristics and 2DEG concentration in the channel are reasonable. The interface trap, located at 0.8 eV below the conduction band edge was used. The areal density of the interface traps used in this work was $2 \times 10^{12}/\mathrm{cm}^2$. The acceptor trap concentration in the buffer layer is $1 \times 10^{18}/\mathrm{cm}^2$ at a trap energy location of 1 eV below the conduction band edge. The capture cross-sections for electrons and holes are $1 \times 10^{-15}/\mathrm{cm}^2$ with a degeneracy factor of one. The models incorporated for the simulations are: FERMI for the fermi statistics model; SRH for the carrier generation and recombination model; FLDMOB and ALBRCT to account for the mobility and saturation velocity effects; GANSAT for the nitride-specific mobility model; the IMPACT SELB impact ionization model for activating avalanche breakdown simulations; the trap model to configure the trap effects; and CALC.STRAIN to calculate the strain and the POLARIZATION model are invoked for epitaxial strain due to the lattice mismatch and spontaneous polarization.

Table 1. Calibration semiconductor parameters for GaN and AlGaN.

Parameters	GaN	AlGaN
Eg300 (eV)	3.4	3.96
Affinity (eV)	–	3.82
Align	0.8	0.8
Permittivity	9.5	9.5
Mun (cm^2/V-s)	900	600
Mup (cm^2/V-s)	10	10
Vsatn (cm/s)	2×10^7	–
Nc300 (/cm^3)	1.07×10^{18}	2.07×10^{18}
Nv300 (/cm^3)	1.16×10^{18}	1.16×10^{18}

The critical variables associated with the device geometry parameters for optimization include the thickness of the gate (T_G), effective length of the field plate (L_{FP}), and the quantity of floating field plate stacks (nFFP). The FP structure conforms with the trend verified by Shreepad Karmalkar et al. [9] that the longer FP's effective length pursues a higher BV. It is feasible to qualitatively anticipate several important trends in the behavior of the BV as a function of the three variables, T_G, L_{FP}, and nFFP by simulations with one variable changed at a time in the individual test. For verifying the superiority of the FFP structure, the GFP structure is firstly optimized to the highest BV condition. Then, the nFFP is set in the FFP structure to ensure the same FP's effective length as the GFP structure to configure the most suitable FFP structure.

The optimum thickness of gate is obtained from the simulation of BV as a function of T_G with other variables constant. In Figure 2a, the effect of varying the T_G is present to confirm the trend that BV declines dramatically as T_G increased more than 0.05 µm. With the T_G increasing, the distance between the FP and the channel gets further, so that the electric field modulation ability of FP for channel gradually decline. Considering the actually manufacturing process of gate metal, the optimum T_G is supposed to be chosen as 0.05 µm.

The optimum length of the field plate is required to achieve the maximum BV with a constant T_G at the optimum value (i.e., T_G = 0.05 µm). The result in Figure 2b implies that the modulation of L_{FP} is actually a balance process. The field distribution along with the 2DEG consists of two electric field peaks near the drain-side edge of the gate and the field plate. The short L_{FP} causes the electric field peak in the edge of the gate dominating the electric field intensity along the 2DEG. In contrast, the field plate's edge appears to have a high electric field peak. The BV firstly presents a rise then a falling trend with the L_{FP} increasing which directly indicates the optimum L_{FP} of 0.8 µm.

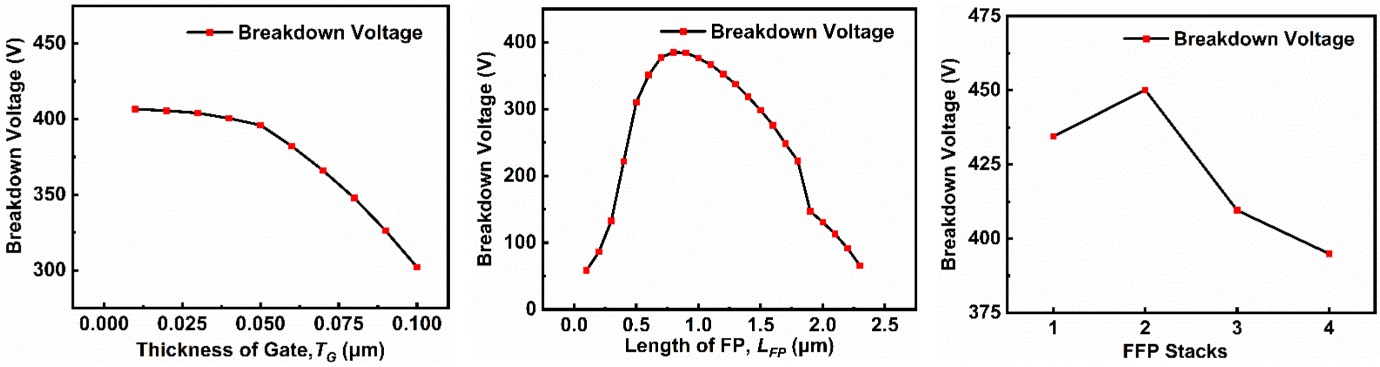

(**a**) (**b**) (**c**)

Figure 2. BV varies as a function of (**a**) T_G, (**b**) L_{FP}, and (**c**) nFFP.

After determining the optimum GFP structure parameters, the same effective length of field plate is controlled to optimize the quantity of the FFP. For the FFP structure, the effective field plate length can be calculated by Equation (1).

$$L_{FP} = L_{GFP} + \sum_{i=1}^{n} L_{spacing,n} + \sum_{i=1}^{n} L_{FFP,n} \tag{1}$$

After a series of different FFP stack simulation experiments, the FFP stacks' length and spacing are set as 150 nm and 50 nm for the highest BV, respectively. Figure 2c shows the dependence of the quantity of FFP stacks with the BV which reveals that the highest breakdown voltage is realized when the quantity of the stacks equals two. The optimum geometry structures of the gate are applied in the simulations and are illustrated in Figure 2a,b. For GFP HEMT, the L_{FP} is optimized to 0.8 µm. To control the same FP's effective length, the L_{GFP} is set as 0.4 µm with the 150 nm floating stack length (i.e., $L_{FFP,1}$ and $L_{FFP,2}$) and 50 nm spacing (i.e., $L_{\mathrm{spacing},1}$ and $L_{\mathrm{spacing},2}$),in the 2FFP structure as shown in Figure 1c.

3. Simulation Results and Discussion

3.1. DC Characteristics

In Figure 3a, the typical DC transfer characteristics and G_{m} curves of the basic, GFP, and 2FFP structure HEMT devices are shown. The results reveal that the threshold voltages of the devices are not impacted significantly on account of the FP structure. As extracted from the results, the drain current at V_{gs} = 3 V is 0.750 A for the basic structure, and that of 0.746 A for the GFP structure, compared with that of 0.748 A for the 2FFP structure. There exists a decrease in the drain current in the GFP and 2FFP devices, which is attributed to the extension part of the gate which is equivalent to the enlargement of the effective gate length, thus causing the current degradation [29]. The maximum G_{m} of the basic, GFP, and 2FFP HEMTs are 383.8 mS/mm, 382.5 mS/mm and 386.7 mS/mm, respectively.

Figure 3b,c demonstrates the breakdown curves of the basic, GFP and 2FFP structures in the OFF-state and the electric field distribution along the 2DEG channel length. In this work, the BV is extracted from the intersection of the saturation segment and the rapidly rising segment due to the impact ionization [9]. When high voltage is biased on the drain electrode, the floating field plate stacks will be induced, become equipotential bodies, and possess different voltages. These stacks can receive the electric field line from the channel and alleviate the electric field crowed at the edge of gate and GFP. As shown in Figure 3d, compared to the conventional GFP, the 2FFP device appears to have four electric field peaks, and the FFP stacks can help the electric field relax in the channel. The

2FFP structure exhibits a 454.4 V breakdown voltage which is 60.1 V higher than the GFP structure. Compared with the 2FFP structure, basic and GFP devices comprehensively perform a higher electric field intensity in the 2DEG channel. This is because the 2FFP structure has more electric field peaks due to the charge induction between each FFP stack. As a consequence, more charged stack edges are generated and they redistribute and reduce the electric field intensity peak there. As a result, the electric field distribution of 2FFP devices becomes smoother than the other structures, which means that 2FFP devices have the best electric field modulation function. The improvement in the BV makes higher drain bias possible, yielding better power performance with brilliant reliability.

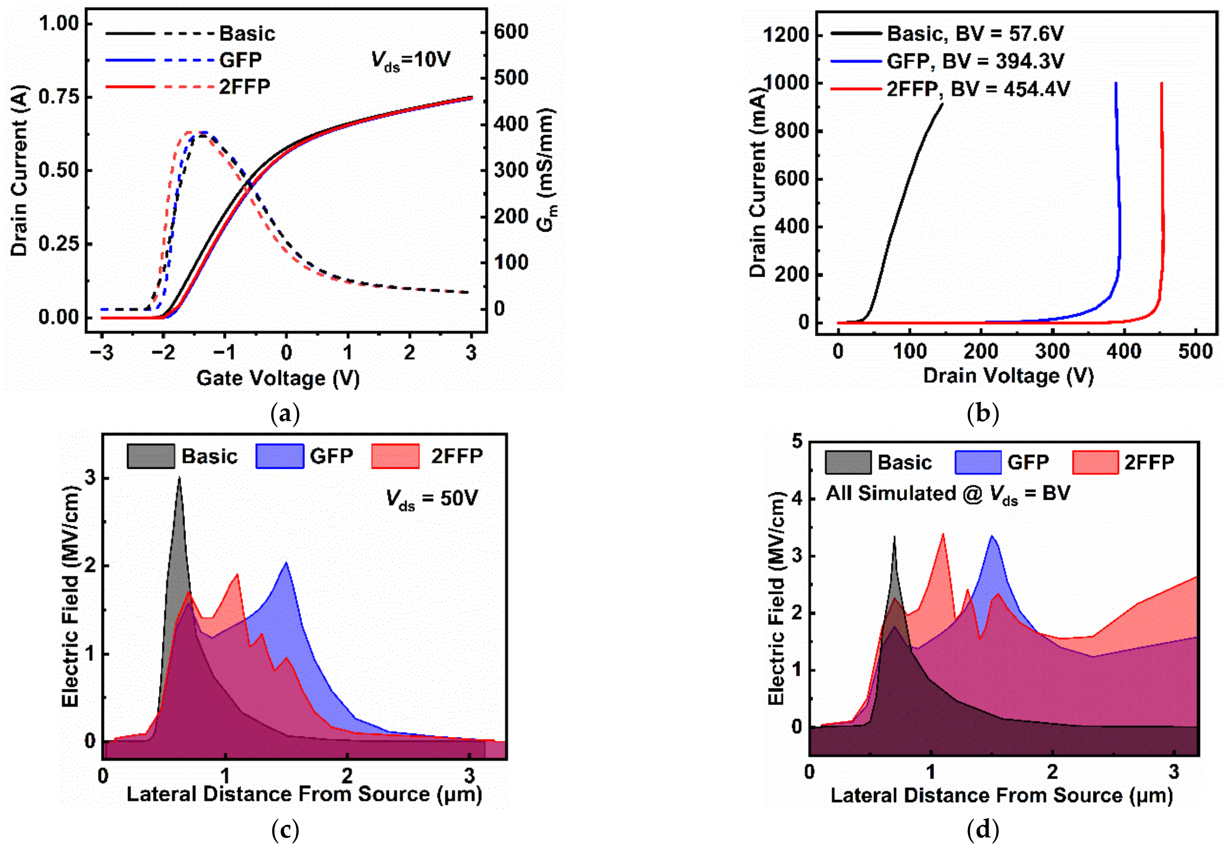

Figure 3. (**a**) Transfer characteristics and G_m curves, (**b**) OFF-state breakdown characteristics, (**c**) electric field distribution at V_{ds} = 50 V, and (**d**) electric field distribution in the OFF-state and V_{ds} = BV condition along the channel of the basic, GFP, and 2FFP HEMTs.

3.2. Transient Characteristic

On account of the surface lattice dislocations, dangling bond, and other damage during the fabrication process, a high density of donor-like traps, also known as surface states, are located at the surface of AlGaN. Due to the high electric field intensity stress under the drain-side edge of the gate in the OFF-state, the electrons inject from the gate and move across the metal/semiconductor interface by tunneling and thermal emission as shown in Figure 4a. These injected electrons are trapped by the donor-like traps leading to a reduction in 2DEG with the traction impact of a high horizontal electric field between the drain and gate. However, trapped electrons during the OFF-state stress in 2FFP structure devices are much less frequent than those in the basic and GFP structure because of the better electric field modulation in 2FFP structure devices. When it turns to ON-state, the electrons injected from the gate are reduced greatly owing to the lower electrical field at the gate's edge. So, the electrons' emission and recombination processes are terminated. The electrons trapped in the donor-like traps detrap and move back into the channel as shown in Figure 4b.

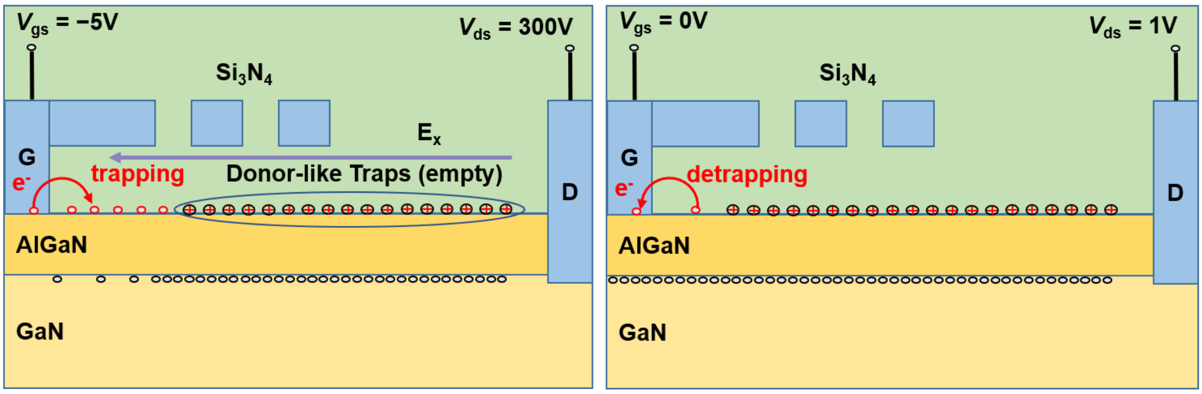

(**a**) (**b**)

Figure 4. Schematic diagrams of (**a**) the OFF-state electrons inject-out process and (**b**) the ON-state electron inject-in process in the 2FFP structure.

The extent of the current collapse phenomenon can be discussed using the ON-resistance increase ratio (i.e., $(R_{\text{on, dynamic}} - R_{\text{on, static}})/R_{\text{on, static}}$) which can be used to assess the basic, GFP, and 2FFP structure suppression capability results. The results are carried out by pulsed measurements, where the gate voltage switches from the ON-state (V_{gs} = 2 V) to the OFF-state (V_{gs} = −5 V) and then to the ON-state (V_{gs} = 2 V), while applying a drain bias voltage V_{ds} from 20 V to 300 V with the increase step of 20 V for each test in the OFF-state. The two ON-states and the OFF-state duration times are fixed at 1ms as shown in Figure 5a. With the OFF-state stress V_{ds} increasing, higher electric field peaks appear at the drain-side edge of the gate. Therefore, more electrons will be injected and the ON-state resistance will increase more acutely. The increase in the ON-resistance ratio is dramatically suppressed by the GFP and 2FFP structure compared with the basic structure as shown in Figure 5b. Due to the high electric field peak appearing at the drain-side edge of the gate, the basic structure performs the most serious current collapse phenomenon when V_{ds} = 20 V and 40 V before the breakdown bias (i.e., V_{ds} < 57.6 V). The advanced current collapse suppression ability of 2FFP devices compared with GFP devices is revealed when the OFF-state stress V_{ds} is higher than 200 V because of the better electric field relaxation of the 2FFP structure. The ON-resistance increase ratio reaches 49.8% for the GFP structure which is much higher than that of the 2FFP structure ~19.9% when the OFF-state V_{ds} = 300 V. From these results, the 2FFP devices perform the highest current collapse suppression ability compared with the basic and GFP devices. As Figure 5c has shown, when the devices are in the ON-state, the conduction band energy at the interface of the heterojunction is lower than the fermi-level (i.e., 0 eV) so that the electrons will be accumulated there. When it is switched to the OFF-state, the energy band will have a different extent rise for GFP and 2FFP devices. In addition, the conduction band energy will be lifted up above the fermi level. Therefore, the electrons will be trapped into the traps due to the surface state.

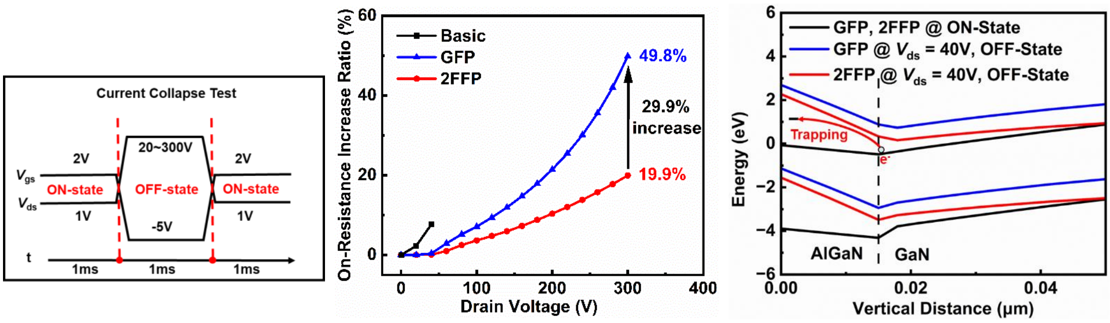

(**a**) (**b**) (**c**)

Figure 5. (**a**) Timings and parameter settings in the current collapse measurements, (**b**) relationship

between the ON-resistance increase ratio caused by the current collapse phenomenon and the applied voltage as a function of the basic, GFP, and 2FFP structures, and (**c**) conduction/valence band energy of the GFP and 2FFP devices during the ON-state and OFF-state extracted from the upper bound of AlGaN to the lower bound of GaN at the drain-side edge of the gate.

3.3. RF Characteristics

The parasitic capacitances C_{gs} and C_{gd} versus V_{ds} varying from 10 V to 30 V are shown in Figure 6a, which reveals the excellent RF performance of the 2FFP structure because of low parasitic capacitances. All of the the results are extracted at a 6 GHz AC small signal condition and the set V_{gs} = −1 V. The results show that C_{gd} gradually decreases with the increase in V_{ds} and the C_{gs} behaviors are the opposite, conforming to the conclusion reported by Che-Yang Chiang et al. [29]. FP-based HEMTs perform higher parasitic capacitances than those of basic HEMT structures due to the additional induced capacitance from the field plate structure. The basic structure shows the base line level of parasitic capacitances, along with C_{gs} = 0.56 pF and C_{gd} = 0.08 pF when V_{ds} = 10 V. The C_{gs} and C_{gd} in the 2FFP structure are 1.03 pF and 0.13 pF, respectively, extracted at V_{ds} = 10 V, and they are lower than those from the GFP HEMT (i.e., C_{gs} = 1.89 pF and C_{gd} = 0.18 pF), revealing the abundant high frequency application field potential in the 2FFP structure.

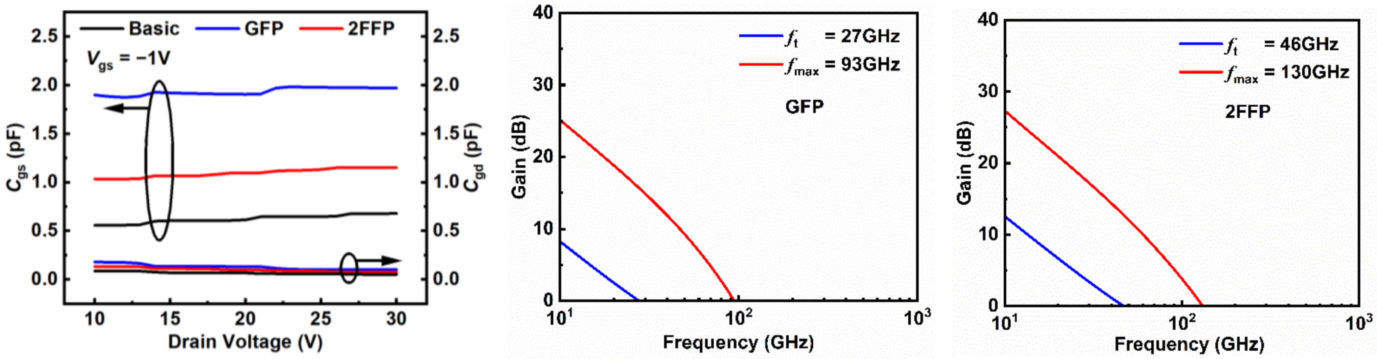

Figure 6. (**a**) Parasitic capacitances' varying curves of the basic, GFP, and 2FFP structures and the cut-off frequency and maximum oscillation frequency of (**b**) GFP HEMT and (**c**) 2FFP HEMT.

The typical small signal characteristics for the GFP and 2FFP structure devices can be seen in Figure 6b,c. The cut-off frequency f_t value is extracted from the extrapolation of the $|H_{21}|^2$ parameter, where its slope equals −20 dB/dec and reaches the gain of 0 dB. The maximum oscillation frequency f_{max} value is extracted from the unilateral power gain, where its slope equals −20 dB/dec and reaches the gain of 0 dB. Compared with GFP structure HEMT device, the 2FFP structure device possesses higher f_t and f_{max} values of 46 GHz and 130 GHz, respectively, which are almost one and a half times higher than those of GFP HEMT.

The additional FP functions as the insertion of parasitic capacitances among all of the electrodes so that it restrains the device's performances under small signal RF conditions, causing lower f_t and f_{max}. Especially in mm-wave devices which have a shorter L_G and channel length, f_t and f_{max} are considerably sensitive to the parasitic capacitances (i.e., C_{gs} and C_{gd}). The equations for f_t and f_{max} are Equations (2) and (3) [30].

$$f_t = \frac{g_m}{2\pi\left(C_{gs} + C_{gd}\right)} \tag{2}$$

$$f_{max} = \frac{f_T}{2\sqrt{(R_i + R_s + R_g)/\left(R_{ds} + 2\pi f_T R_g C_{gd}\right)}} \tag{3}$$

The device with the 2FFP structure features lower C_{gd} and C_{gs} than the GFP structure, with it acquiring excellent RF performance accompanied by an increased breakdown voltage. The Johnson figure of merit (JFOM) is a commonly used parameter to judge RF GaN devices. The JFOM is depicted in Equation (4) [31]. Compared with the JFOM of the GFP device, which is 10.65 THz·V, the proposed 2FFP device performs almost two times better in terms of the JFOM. Therefore, the potential of the 2FFP structure in RF GaN is obvious. The results are summarized in Table 2.

$$JFOM = f_t \times BV \tag{4}$$

Table 2. BV, f_t, and JFOM calculated summary for basic, GFP, and 2FFP structures.

Devices	BV (V)	f_t (GHz)	JFOM (THz·V)
basic	57.6	93	1.03
GFP	394.3	27	10.65
2FFP	454.4	46	20.90

Some FP and gate structure works have also been reported earlier in [32,33] where different gate structure configurations were investigated for DC and RF performance. The performance comparison for different types of gate structures, field plates, and the proposed 2FFP structure is shown in Table 3. The 2FFP structure performs the better among these device structures. For RF GaN devices, higher g_m, BV, f_t and f_{max} are pursued where all the goals are achieved by 2FFP devices and this presents a better alternative.

Table 3. Summary of the device performance parameters of this work compared with previous work.

Parameter	Previous Work [32,33]							Proposed 2FFP
	Type I	Type II	Type III	Type IV	Type V	GFP	GGFP	
g_m (S/mm)	0.29	0.25	0.29	0.28	0.33	0.34	0.35	0.38
BV (V)	–	-	-	-	-	-	270	454
f_t (GHz)	14.14	17.33	21.79	14.52	25.87	17.61	28.34	46
f_{max} (GHz)	35.5	28.2	44.65	35.45	53.1	44	80	130

4. Conclusions

In this paper, a systematic procedure has been carried investigated for a device structure optimization method which investigates the thickness of the gate, the effective length of the FP, and the quantity of FFP stacks to obtain the maximum BV. Based on the optimized 2FFP, GFP, and basic structure HEMTs, the transfer characteristic, breakdown voltage, parasitic capacitance, and frequency response were analyzed and discussed. The geometry parameters of optimized AlGaN/GaN HEMTs are verified by applying SILVACO ATLAS 2D simulation. In the 2FFP structure, the increased BV of 454.4 V, the excellent current collapse suppression effect, the low parasitic capacitance C_{gs} of 1.03 pF and C_{gd} of 0.13 pF, and the improved f_t = 46 GHz and f_{max} = 130 GHz were achieved. The 2FFP structure realizes the increased BV as well as the suppressed RF characteristics' degradation, which are not realizable for GFP structure HEMT. It was observed that the 2FFP structure demonstrates a robust potential in RF-scale GaN HEMT compared with the conventional gate field plate structure.

Author Contributions: Conceptualization, P.W. and Q.W.; methodology, P.W. and C.D.; software, P.W. and H.C.; validation, C.D., W.C., C.T., C.G., and N.T.; formal analysis, P.W. and C.D.; investigation, P.W., H.C. and F.D.; data curation, H.C. and F.D.; writing—original draft preparation, P.W.; writing—review and editing, C.D. and Q.W.; project administration, Q.W.; funding acquisition, H.Y. and Q.W. All authors have read and agreed to the published version of the manuscript.

Funding: This work was funded by the fabrication of normally-off GaN devices based the on in situ SiNx passivation and selective area growth recessed-gate techniques and the reliability study (National Natural Science Foundation of China, Grant No: 62274082), research on novelty low-resistance source/drain ohmic contact for GaN p-FET (Grant No. JCYJ20220530115411025), research on the fabrication and mechanism of GaN power and RF devices (Grant No. JCYJ20200109141233476), research on the GaN chip for 5G applications (Grant No. JCYJ20210324120409025), research on highly reliable GaN power devices and related industrial power systems (Grant No. HZQB-KCZYZ-2021052), and Special Funds for the Cultivation of Guangdong College Students' Scientific and Technological Innovation. ("Climbing Program" Special Funds) pdjh2023c21501.

Institutional Review Board Statement: Not applicable.

Informed Consent Statement: Not applicable.

Data Availability Statement: The data presented in this study are available on request from the corresponding author.

Conflicts of Interest: The authors declare no conflict of interest. The funders had no role in the design of the study; in the collection, analysis, or interpretation of data; in the writing of the manuscript; or in the decision to publish the results.

References

1. Xing, H.; Keller, S.; Wu, Y.-F.; McCarthy, L.; Smorchkova, I.P.; Buttari, D.; Coffie, R.; Green, D.S.; Parish, G.; Heikman, S.; et al. Gallium nitride based transistors. *J. Phys. Condens. Matter* **2001**, *13*, 7139. [CrossRef]
2. Eastman, L.; Mishra, U. The toughest transistor yet [GaN transistors]. *IEEE Spectr.* **2002**, *39*, 28–33. [CrossRef]
3. Zhang, N.; Mehrotra, V.; Chandrasekaran, S.; Moran, B.; Shen, L.; Mishra, U.; Etzkorn, E.; Clarke, D. Large area GaN HEMT power devices for power electronic applications: Switching and temperature characteristics. In Proceedings of the IEEE 34th Annual Conference on Power Electronics Specialist 2003—PESC'03, Acapulco, Mexico, 15–19 June 2003; IEEE: Piscataway, NJ, USA, 2003; Volume 1. [CrossRef]
4. Mishra, U.K.; Parikh, P.; Wu, Y.-F. AlGaN/GaN HEMTs-an overview of device operation and applications. *Proc. IEEE* **2002**, *90*, 1022–1031. [CrossRef]
5. Xing, H.; Dora, Y.; Chini, A.; Heikman, S.; Keller, S.; Mishra, U. High Breakdown Voltage AlGaN–GaN HEMTs Achieved by Multiple Field Plates. *IEEE Electron Device Lett.* **2004**, *25*, 161–163. [CrossRef]
6. Kong, X.; Wei, K.; Liu, G.-G.; Liu, X.-Y. Improvement of breakdown characteristics of an AlGaN/GaN HEMT with a U-type gate foot for millimeter-wave power application. *Chin. Phys. B* **2012**, *21*, 128501. [CrossRef]
7. Moon, J.; Grabar, R.; Antcliffe, M.; Fung, H.; Tang, Y.; Tai, H. High-speed FP GaN HEMT with f_T/f_{MAX} of 95/200 GHz. *Electron. Lett.* **2018**, *54*, 657–659. [CrossRef]
8. Zhang, Y.; Wei, K.; Huang, S.; Wang, X.; Zheng, Y.; Liu, G.; Chen, X.; Li, Y.; Liu, X. High-Temperature-Recessed Millimeter-Wave AlGaN/GaN HEMTs with 42.8% Power-Added-Efficiency at 35 GHz. *IEEE Electron Device Lett.* **2018**, *39*, 727–730. [CrossRef]
9. Karmalkar, S.; Mishra, U. Enhancement of breakdown voltage in AlGaN/GaN high electron mobility transistors using a field plate. *IEEE Trans. Electron Devices* **2001**, *48*, 1515–1521. [CrossRef]
10. Amit; Rawal, D.S.; Sharma, S.; Kapoor, S.; Liashram, R.; Chaubey, R.K.; Vinayak, S.; Sharma, R.K. Design and Fabrication of Multi-finger Field Plate for Enhancement of AlGaN/GaN HEMT Breakdown Voltage. *Def. Sci. J.* **2018**, *68*, 290–294. [CrossRef]
11. Lian, Y.-W.; Lin, Y.-S.; Lu, H.-C.; Huang, Y.-C.; Hsu, S.S.H. Drain E-Field Manipulation in AlGaN/GaN HEMTs by Schottky Extension Technology. *IEEE Trans. Electron Devices* **2015**, *62*, 519–524. [CrossRef]
12. Bahat-Treidel, E.; Hilt, O.; Brunner, F.; Sidorov, V.; Würfl, J.; Tränkle, G. AlGaN/GaN/AlGaN DH-HEMTs Breakdown Voltage Enhancement Using Multiple Grating Field Plates (MGFPs). *IEEE Trans. Electron Devices* **2010**, *57*, 1208–1216. [CrossRef]
13. Luo, J.; Zhao, S.-L.; Lin, Z.-Y.; Zhang, J.-C.; Ma, X.-H.; Hao, Y. Enhancement of Breakdown Voltage in AlGaN/GaN High Electron Mobility Transistors Using Double Buried p-Type Layers. *Chin. Phys. Lett.* **2016**, *33*, 067301. [CrossRef]
14. Bahat-Treidel, E.; Brunner, F.; Hilt, O.; Cho, E.; Wurfl, J.; Trankle, G. AlGaN/GaN/GaN:C Back-Barrier HFETs with Breakdown Voltage of Over 1 kV and Low $R_{ON} \times A$. *IEEE Trans. Electron Devices* **2010**, *57*, 3050–3058. [CrossRef]
15. Bahat-Treidel, E.; Hilt, O.; Brunner, F.; Wurfl, J.; Trankle, G. Punchthrough-Voltage Enhancement of AlGaN/GaN HEMTs Using AlGaN Double-Heterojunction Confinement. *IEEE Trans. Electron Devices* **2008**, *55*, 3354–3359. [CrossRef]
16. Murugapandiyan, P.; Mohanbabu, A.; Lakshmi, V.R.; Wasim, M.; Sundaram, K.M. Investigation of Quaternary Barrier InAlGaN/GaN/AlGaN Double-Heterojunction High-Electron-Mobility Transistors (HEMTs) for High-Speed and High-Power Applications. *J. Electron. Mater.* **2019**, *49*, 524–529. [CrossRef]
17. Wang, Z.; Cao, J.; Sun, R.; Wang, F.; Yao, Y. Numerical investigation on AlGaN/GaN short channel HEMT with AlGaN/InGaN/AlGaN quantum well plate. *Superlattices Microstruct.* **2018**, *120*, 753–758. [CrossRef]
18. Wang, Z.; Zhang, Z.; Wang, S.; Chen, C.; Wang, Z.; Yao, Y. Design and Optimization on a Novel High-Performance Ultra-Thin Barrier AlGaN/GaN Power HEMT with Local Charge Compensation Trench. *Appl. Sci.* **2019**, *9*, 3054. [CrossRef]

19. Zhang, S.; Wei, K.; Ma, X.; Zhang, Y.C.; Lei, T. Millimeter-wave AlGaN/GaN HEMT breakdown voltage enhancement by a recessed float field plate. *Appl. Phys. Express* **2019**, *12*, 054007. [CrossRef]
20. Wu, W.-H.; Lin, Y.-C.; Chin, P.-C.; Hsu, C.-C.; Lee, J.-H.; Liu, S.-C.; Maa, J.-S.; Iwai, H.; Chang, E.Y.; Hsu, H.-T. Reliability improvement in GaN HEMT power device using a field plate approach. *Solid-State Electron.* **2017**, *133*, 64–69. [CrossRef]
21. Kurbanova, N.E.; Demchenko, O.I.; Velikovskiy, L.E.; Sim, P. Field-plate design optimization for high-power GaN high electron mobility transistors. In Proceedings of the 2017 International Siberian Conference on Control and Communications (SIBCON), Astana, Kazakhstan, 29–30 June 2017; IEEE: Piscataway, NJ, USA, 2017.
22. Chitransh, A.; Moonka, S.; Priya, A.; Prasad, S.; Sengupta, A.; Islam, A. Analysis of breakdown voltage of a field plated High Electron Mobility Transistor. In Proceedings of the 2017 Devices for Integrated Circuit (DevIC), Kalyani, India, 23–24 March 2017; IEEE: Piscataway, NJ, USA, 2017.
23. Mase, S.; Egawa, T.; Wakejima, A. Transient characteristics of AlGaN/GaN high-electron-mobility transistor with bias-controllable field plate. *Appl. Phys. Express* **2015**, *8*, 036601. [CrossRef]
24. Koudymov, A.; Adivarahan, V.; Yang, J.; Simin, G.; Khan, M. Mechanism of current collapse removal in field-plated nitride HFETs. *IEEE Electron Device Lett.* **2005**, *26*, 704–706. [CrossRef]
25. Brannick, A.; Zakhleniuk, N.A.; Ridley, B.K.; Shealy, J.R.; Schaff, W.J.; Eastman, L.F. Influence of Field Plate on the Transient Operation of the AlGaN/GaN HEMT. *IEEE Electron Device Lett.* **2009**, *30*, 436–438. [CrossRef]
26. Saito, W.; Kakiuchi, Y.; Nitta, T.; Saito, Y.; Noda, T.; Fujimoto, H.; Yoshioka, A.; Ohno, T.; Yamaguchi, M. Field-Plate Structure Dependence of Current Collapse Phenomena in High-Voltage GaN-HEMTs. *IEEE Electron Device Lett.* **2010**, *31*, 659–661. [CrossRef]
27. Hasan, T.; Asano, T.; Tokuda, H.; Kuzuhara, M. Current Collapse Suppression by Gate Field-Plate in AlGaN/GaN HEMTs. *IEEE Electron Device Lett.* **2013**, *34*, 1379–1381. [CrossRef]
28. *ATLAS User's Manual*; Silvaco Int.: Santa Clara, CA, USA, 2010.
29. Chiang, C.-Y.; Hsu, H.-T.; Chang, E.Y. Effect of Field Plate on the RF Performance of AlGaN/GaN HEMT Devices. *Phys. Procedia* **2012**, *25*, 86–91. [CrossRef]
30. Bhat, A.M.; Shafi, N.; Sahu, C.; Periasamy, C. Analysis of AlGaN/GaN HEMT and Its Operational Improvement Using a Grated Gate Field Plate. *J. Electron. Mater.* **2021**, *50*, 6218–6227. [CrossRef]
31. Fletcher, A.S.A.; Nirmal, D.; Ajayan, J.; Arivazhagan, L. An Intensive Study on Assorted Substrates Suitable for High JFOM AlGaN/GaN HEMT. *Silicon* **2020**, *13*, 1591–1598. [CrossRef]
32. Toprak, A.; Osmanoğlu, S.; Öztürk, M.; Yılmaz, D.; Cengiz, Ö.; Şen, Ö.; Bütün, B.; Özcan, Ş.; Özbay, E. Effect of gate structures on the DC and RF performance of AlGaN/GaN HEMTs. *Semicond. Sci. Technol.* **2018**, *33*, 125017. [CrossRef]
33. Subramani, N.K.; Couvidat, J.; Al Hajjar, A.; Nallatamby, J.-C.; Sommet, R.; Quere, R. Identification of GaN Buffer Traps in Microwave Power AlGaN/GaN HEMTs through Low Frequency S-Parameters Measurements and TCAD-Based Physical Device Simulations. *IEEE J. Electron Devices Soc.* **2017**, *5*, 175–181. [CrossRef]